

# *ForEdgeClim*

Emma Van de Walle - Q-ForestLab

August 2025



In this report an overview of the model *ForEdgeClim* is written down. *ForEdgeClim* is a process-based microclimate model that is initially written to simulate microclimate gradients along transect lines from a forest's core towards its edge.

The model follows a mechanistic approach to microclimate modelling, grounded on the principle of energy conservation. Semi-opaque surfaces in the environment, such as the canopy and the ground, absorb solar radiation while simultaneously emitting thermal radiation. These surfaces also exchange sensible heat with the air and experience latent heat fluxes (here, cooling by evapotranspiration). Additionally, the ground stores and releases energy, contributing to the overall energy balance.

Since each component of the energy budget depends on temperature, they are all included in an iterative loop until energy balance convergence is reached and this for a steady state, single moment in time. [Note: this convergence is pursued for the surface (i.e., forest structural) temperature. Air and soil surface temperature are modelled as well, but are updated by the updated surface temperature. Therefore, there is no convergence criterion for air and soil surface temperature. (See further for more explanation.)]

The assumption of a steady state condition is valid here because our objective is to model temperature between consecutive hourly time steps, and thermal equilibrium is reached much faster than the hourly time step we apply. There is therefore no temporary heat accumulation or delayed temperature response. We could make the model dynamic, which could be interesting for studying temporal dynamics related to heat storage or soil dynamics. However, our current focus is on modelling temperature through processes such as radiation, latent heat, sensible heat, and ground heat flux, all of which reach equilibrium more quickly than the hourly time step.

The use of an iterative loop is necessary because no closed-form mathematical solution exists for the energy budget equations. All processes in the microclimate model continuously influence each

other, and only through repeated updates can a stable and physically realistic temperature distribution be achieved. One of the complex interdependencies is for example the relationship between surface heating and sensible heat exchange.

The model starts by simulating shortwave radiative transfer (RTM) that calculates shortwave radiation in two directions: vertical and lateral. The RTM is therefore two-dimensional. Next, it attempts to close the energy balance by reducing the energy balance closure error to less than  $E_{bal}$ , an equilibrium criterion variable (e.g.  $1 \text{ W/m}^2$ ). This equation (eq. 1) balances the net radiation ( $R_n$ ), sensible heat flux ( $H$ ), latent heat flux ( $LE$ ), and ground heat flux ( $G$ ) for the forest structure. Ground heat flux ( $G$ ) is 0 everywhere except for the soil. It is (currently) only used to simulate soil surface temperature, which in turn influences air temperature. Net radiation consists of both shortwave and longwave radiation in 2D. Sensible heat flux is calculated in 3D, whereas latent heat flux and ground heat flux are calculated in 1D (vertically). The processes are carried out between voxels in 3D. Each voxel contains a density value, determined from terrestrial laser scanning (TLS) data to account for the forest structure. The density of each voxel is normalised and ranges between 0 and 1. Structural data, measured with the TLS scanner, have been collected monthly since March 2023. When voxel densities are normalised to values between 0 and 1, the normalisation is applied across all months combined, rather than separately for each month. Consequently, the month with the highest density values contains voxels with values equal to 1, while voxels from all other months never reach 1. The normalisation procedure is as follows. First, voxel densities are normalised separately for each month, resulting in 3D grids with voxel values ranging from 0 to 1. Next, the mean hinge-PAI across all scan positions is calculated for each month using the Python package *PyLidar*. The month with the highest mean hinge-PAI ( $PAI_{max}$ ) is left unadjusted, while all other months are further corrected by multiplying their voxel values by the ratio  $\frac{PAI_{month}}{PAI_{max}}$ .

$$E_{bal} = R_n - H - LE - G = 0 \quad (1)$$

## Modelling temperatures

As mentioned before, *ForEdgeClim* models three temperature values. First and foremost, the surface temperature  $T_f$  is modelled. This temperature represents the temperature of the forest surface structures within the voxel grid, i.e., leaves, branches and stems. In the model, Newton's method is applied, as described above, to update the surface temperature between successive iteration steps.

In addition to surface temperature, both air temperature  $T_{air}$  and soil surface temperature  $T_s$  are modelled. Air temperature represents the temperature of the air within each voxel. Since each voxel has a certain density value representing the structure, the remaining density (1 - density) represents the air. Soil surface temperature is a single-layer temperature, effectively representing the ground surface temperature. Below, further explanation is provided on how air and soil surface temperature are modelled.

### Air temperature

Modelling air temperature is done via a linearisation, similar to the approach used in the microclimate model *microclimf* by Ilya Maclean. This method is mostly valid when there are small temperature differences between air temperature and surface temperature, when there is sufficient air streaming, when the net radiation or the humidity is not extreme and when the forest structure is quite homogeneous.

Air temperature is derived as shown in eq. 2. In this equation  $w$  refers to weight,  $g$  to convection and  $T$  to temperature. The subscript  $m$  refers to macroenvironment,  $s$  to soil and  $f$  to forest surface.  $mX$  and  $mZ$  further refer to the macroenvironment along the X-axis (lateral) and the Z-axis (vertical), respectively.

The weights  $w$  are defined as exponential weightings of the boundary distances. All definitions of  $w$  have the same structure, an example for  $w_s$  is given in eq. 3. Here,  $d_s$  is the distance to the forest soil surface and  $\alpha_s$  is defined in eq. 4. In eq. 4,  $i_s$  is the 'distance of influence'.  $i_s$  is defined as the distance over which the influence of soil surface temperature on air temperature is reduced by 50%. Exponential weighting is well-suited for microclimate modelling as it naturally represents the gradual decline in influence with distance, aligning with physical heat transfer principles. It ensures smooth transitions between temperature sources, accommodates varying spatial scales, and integrates well with convection and conduction processes. Additionally, it prevents unrealistic temperature fluctuations and maintains numerical stability.

The convective  $g$  and the distances of influence  $i$  are input parameters and  $T_f$  is the to be modelled forest surface temperature. If a voxel does not contain forest structure (and therefore has no  $T_f$ ), the average surface temperature of the corresponding X-, Y- and Z-planes is used.

$$T_{air} = \frac{(w_{mX} + w_{mZ}) \cdot g_m \cdot T_m + w_s \cdot g_s \cdot T_s + w_f \cdot g_f \cdot T_f}{(w_{mX} + w_{mZ}) \cdot g_m + w_s \cdot g_s + w_f \cdot g_f} \quad (2)$$

$$w_s = e^{\alpha_s \cdot d_s} \quad (3)$$

$$\alpha_s = \log(0.5)/i_s \quad (4)$$

## Soil surface temperature

The soil surface temperature ( $T_s$ ) is modelled using the heat conduction equation (Fourier's law) in 1D (see eq. 5).  $T_{soil}$  is the mean observed soil temperature at 20 locations within the forest transect, measured at a depth of 6cm. This value is assumed to be stable over a time bin of around 6h.  $z$  is the depth at which this stable temperature is measured, i.e., 6cm,  $G$  is the ground heat flux and  $k_s$  the thermal conductance of the soil.  $G$  is explained further down.

$$T_s = T_{soil} + \frac{G \cdot z}{k_s} \quad (5)$$

## Radiative transfer model

The radiative processes are simulated in 2D (vertical and lateral) and use the two-stream radiative transfer model, based on the version also used in the ED 2.2 model. (See the report [Two-stream Radiative Transfer Model of ED 2.2](#) for a detailed description of the model.)

In short, for the shortwave RTM, the model simulates multi-scatter radiative transfer along a single column or row, where direct and diffuse sunlight interact with a layered structure containing density values. Direct beam radiation ( $I_b^\downarrow$ ) is represented by an exponential decaying process, and the RTM solves for diffuse upward and downward radiation ( $I^\downarrow$  and  $I^\uparrow$ ) in each canopy layer using a linear matrix equation. Equations 6, 7 and 8 present the equations for the direct and diffuse radiation components. Table 5 includes and explains the parameters used in these equations.

$$\frac{dI_b^\downarrow}{dx} = -K_b I_b^\downarrow \quad (6)$$

$$\frac{dI^\downarrow}{dx} = -[1 - (1 - \beta)\omega]K_d I^\downarrow + \beta\omega K_d I^\uparrow + (1 - \beta_0)\omega K_b I_{sky,b}^\downarrow e^{-K_b x} \quad (7)$$

$$\frac{dI^\uparrow}{dx} = [1 - (1 - \beta)\omega]K_d I^\uparrow - \beta\omega K_d I^\downarrow - \beta_0\omega K_b I_{sky,b}^\downarrow e^{-K_b x} \quad (8)$$

The choice of values for the parameters in table 5 is not random. For example, in temperate forests, direct sunlight is significantly weakened by the presence of leaves, branches, and other structures that lie directly in the light path. Values for  $K_b$  in the vertical direction of around 0.90 correspond to the shading and absorption by dense canopies. Diffuse sunlight is less strongly attenuated because it comes from multiple directions and some of it can penetrate through small openings in the canopy. This results in a lower attenuation coefficient. The attenuation coefficients are, in principle, season-dependent; for instance, in winter, the attenuation coefficient can be lower due to the absence of leaves. Lateral attenuation coefficients are lower because light travelling horizontally passes through a shorter path within the tree structure, often encountering fewer obstacles.

The parameters used in eq. 6, 7 and 8, along with the values of direct and diffuse solar radiation from the above canopy and the ground reflectance ( $\omega_g$ ), serve as input parameters for the shortwave two-stream RTM model.

This model is a 'single-column' model. To achieve a 2D RTM for our 3D grid, this model is applied to every vertical column (fixed XY) and every horizontal row (fixed YZ).

## Net radiation $R_n$

Net radiation is described in eq. 9 and consists of three terms derived from the shortwave RTM ( $I_b^\downarrow$ ,  $I^\downarrow$  and  $I^\uparrow$ ), as well as two terms representing incoming and outgoing longwave radiation ( $L^\downarrow$  and  $L^\uparrow$ ). Both longwave radiative terms are described using an analogous two-stream RTM model as described above, for the shortwave radiation. Yet, here, the direct beam radiation terms are removed, and a source of thermally emitted radiation is added. The equations governing the longwave terms are given in eq. 10 and eq. 11. In those equations,  $\epsilon_f$  and  $\sigma$  represent the forest emissivity and the Stephan-Boltzmann constant, respectively. All other parameters are similar as in eq. 7 and 8. The downward longwave radiation at the top of the canopy ( $L_{sky}^\downarrow$ ) is an input driver.

$$R_n = I^\downarrow - I^\uparrow + I_b^\downarrow + L^\downarrow - L^\uparrow \quad (9)$$

$$\frac{dL^\downarrow}{dx} = -[1 - (1 - \beta)\omega]K_d L^\downarrow + \beta\omega K_d L^\uparrow + \epsilon_f \sigma T_f^4 (1 - \beta)\omega K_d \quad (10)$$

$$\frac{dL^\uparrow}{dx} = [1 - (1 - \beta)\omega]K_d L^\uparrow - \beta\omega K_d L^\downarrow + \epsilon_f \sigma T_f^4 (1 - \beta)\omega K_d \quad (11)$$

## Ground heat flux $G$

Ground heat flux is modelled as a percentage ( $p$ ) of the net radiation at ground level and is given in eq. 12 (ref. SCOPE 2.0 model). Here  $\rho$  is the forest density (in the layer just above the ground).

$$G = p \cdot (1 - \rho) \cdot R_n \quad (12)$$

## Sensible heat flux $H$

A surface heated by solar radiation transfers some of this heat to the surrounding air. According to the laws of energy conservation, the air absorbs this heat. This process is known as sensible heat exchange. In *ForEdgeClim* sensible heat exchange is conducted in 3D and simulates 1, heat diffusion ( $D$ ) between the air of adjacent neighbouring voxels using the formula for heat transfer by diffusion (Fourier's law of heat conduction) (eq. 13 and 14) and 2, heat convection (actual sensible heat exchange) from the forest surface to the surrounding air (eq. 15). At the edges of the grid, there is also a transfer of heat with the macroenvironment and forest soil surface.

In eq. 13,  $h$  is the thermal diffusion coefficient of air,  $A$  the surface area of one voxel face and  $\Delta T_{air}$  the difference in air temperature between neighbouring voxels. In eq. 14,  $c_p$  is the specific heat of air,  $\rho_{air}$  the density of air and  $V$  the voxel volume.

In eq. 15,  $g_f$  is the forest convection.

$$D = h \cdot A \cdot \Delta T_{air} \quad (13)$$

$$T_{air-new} = T_{air-old} - \frac{D}{c_p \cdot \rho_{air} \cdot V} \quad (14)$$

$$H = \rho \cdot g_f \cdot (T_f - T_{air}) \quad (15)$$

## Latent heat flux $LE$

Latent heat flux is modelled using the empirical Priestley-Taylor method (eq. 16). This is a simplified version of the Penman-Monteith equation that simulates the potential evapotranspiration and where all aerodynamic variables are encapsulated in a single parameter,  $\alpha$ , the Priestley-Taylor coefficient. In this equation, it is assumed that the aerodynamic term (the advective component) is negligible. As a result, evapotranspiration can be calculated based on the available net radiation energy and the psychrometric constant. It performs well under specific climatic and environmental conditions. These conditions include negligible advective processes, surfaces with unlimited water availability, radiation being the dominant factor for evaporation, and relatively stable atmospheric conditions (i.e., no extreme wind, pressure, or humidity variations).

$$LE = \rho \cdot \alpha \cdot R_n \cdot \frac{s(T_{fc})}{s(T_{fc}) + \gamma} \quad (16)$$

In eq. 16,  $\gamma$  is the psychrometric constant and  $s$  represents the slope of the saturation pressure curve in  $kPa/K$  and is further defined in eq. 17.  $T_{fc}$  is the forest structural temperature expressed in  $^{\circ}C$ . This in contrast with  $T_f$ , which is expressed in K.

$$s(T_{fc}) = 4098 \cdot \frac{e_s(T_{fc})}{(T_{fc} + 237.3)^2} \quad (17)$$

In eq. 17,  $e_s$  is the saturated vapor pressure. It is calculated using the empirical formula by Tetens (see eq. 18). The formula by Tetens is an empirical approximation of the Clausius-Clapeyron equation and works well for temperatures between  $-40^{\circ}C$  and  $50^{\circ}C$ .

$$e_s(T_{fc}) = 0.6018 \cdot \exp\left(\frac{17.27 \cdot T_{fc}}{T_{fc} + 237.3}\right) \quad (18)$$

## Solving the energy balance

Within the iterative loop to converge the energy balance per voxel, and therefore for the entire system, net radiation, sensible heat flux, latent heat flux, ground heat flux, air temperature and soil surface temperature are updated by an updated surface temperature.

Based on the *SCOPE 2.0* model, Newton's method is used to update surface temperature values between successive iteration steps. This method utilizes the energy balance closure error ( $E_{bal}$ ) and its derivative with respect to forest temperature (see eq. 19). In this equation,  $W$  is a weighting for the step size.

$$T_{f-new} = T_{f-old} - W \cdot \frac{E_{bal}(T_f)}{\frac{\delta E_{bal}(T_f)}{\delta T_f}} \quad (19)$$

The derivative of the energy balance closure error to the forest temperature can further be written as: (Remark that there is no derivative of G because G is only calculated for the soil surface and not for the structural surface of the forest.)

$$\frac{\delta E_{bal}(T_f)}{\delta T_f} = \frac{\delta R_n(T_f)}{\delta T_f} - \frac{\delta H(T_f)}{\delta T_f} - \frac{\delta LE(T_f)}{\delta T_f} \quad (20)$$

And from the formulas in the sections above, it follows that eq. 20 can be further expanded as:

$$\frac{\delta E_{bal}(T_f)}{\delta T_f} = -4 \cdot e_f \cdot \sigma \cdot T_f^3 - \rho \cdot g_f - \rho \cdot \alpha \cdot (-4 \cdot e_f \cdot \sigma \cdot T_f^3) \cdot \frac{s}{s + \gamma} + \rho \cdot \alpha \cdot R_n \cdot \frac{dF(T_f)}{dT_f} \quad (21)$$

with

$$\frac{dF(T_{fc})}{dT_{fc}} = \frac{\frac{ds(T_{fc})}{dT_{fc}} \cdot (s + \gamma) - s \cdot \frac{ds(T_{fc})}{dT_{fc}}}{(s + \gamma)^2} \quad (22)$$

and

$$\frac{ds(T_{fc})}{dT_{fc}} = \frac{4098 \cdot \frac{de_s(T_{fc})}{dT_{fc}} \cdot (T_{fc} + 237.2)^2 - 2 \cdot (T_{fc} + 237.3) \cdot 4098 \cdot e_s(T_{fc})}{(T_{fc} + 237.3)^4} \quad (23)$$

and

$$\frac{de_s(T_{fc})}{dT_{fc}} = 0.6108 \cdot \exp\left(\frac{17.27 \cdot T_{fc}}{T_{fc} + 237.3}\right) \cdot \frac{(T_{fc} + 237.3) \cdot 17.27 - 17.27 \cdot T_{fc}}{(T_{fc} + 237.3)^2} \quad (24)$$

in which  $T_{fc}$  is the forest surface temperature in °C.

## Numerical implementation

*ForEdgeClim* employs a grid-based numerical approach to simulate microclimate temperature and energy exchange in fragmented forests. Given the structured nature of the 3D voxel-based representation of the forest, a grid-based method is a logical choice, ensuring spatially explicit calculations and allowing for efficient computation of radiative and heat transfer processes.

The model integrates two numerical methods: the Finite Difference Method (FDM) and the Finite Volume Method (FVM). FDM is utilised for air-to-air convective heat transfer, where temperature gradients are approximated using finite difference schemes. This allows for an efficient discretisation of heat diffusion processes within the voxel grid. Meanwhile, FVM is applied to solve the energy balance equation, ensuring conservation of energy fluxes at the voxel scale. FVM is particularly advantageous in this context as it explicitly accounts for energy exchange between adjacent voxels, which

is essential for accurately modelling the interactions between forest structure, air, and soil surface.

The choice of a grid-based approach over particle methods (like Monte Carlo methods) or mesh-based methods is motivated by the structured nature of forest transects in the model. A voxel-based discretisation aligns well with available 3D structural data, such as LiDAR-derived forest density maps, allowing for direct incorporation of empirical data. Furthermore, grid-based methods facilitate efficient coupling of radiative transfer, heat exchange, and evapotranspiration processes within a unified computational framework. This hybrid FDM-FVM approach balances computational efficiency with physical accuracy, making it well-suited for simulating spatially heterogeneous microclimates in complex forested environments.

## Input drivers, (physical) constants, model parameters, and prognostic variables

An overview of the input drivers, (physical) constants, model parameters and prognostic variables is respectively given in table 6, 7, 5 and 8.

If a table contains the column 'submodel', this refers to the process(es) to which the variable contributes. Submodels can be shortwave RTM (SW RTM), longwave RTM (LW RTM), sensible heat flux (H), latent heat flux (LE), ground heat flux (G), air temperature ( $T_{air}$ ), and soil surface temperature ( $T_s$ ).

The several model parameters can be tweaked to calibrate and validate our model.

## Some first results

The structure grid used in the simulation below is the TLS scan taken from the transect in Gontrode forest in July 2023. An illustration can be found in figure 1 in 2D. The forest edge is located on the right side, in the east, at the maximum X-position. We assume that there is more forest to the north, west, and south. Hence, in the 2D RTM, radiation enters from above and from the right side. In the transect, we observe a gap around the  $X = 50\text{m}$  position. This is due to ash dieback, caused by a chronic fungal disease affecting ash trees in Europe, characterised by leaf loss and crown dieback in infected trees. The transect consists mainly of ash trees between  $X = 0$  and  $X = 50$ , while beyond  $X = 50$ , it is predominantly composed of beech and oak trees. In the figure, we also see a higher structure to the right of the gap. This is the flux tower located within the transect. We furthermore observe a higher density in the upper right part of the gap. Here, a healthy oak is taking advantage of the ash dieback to expand its canopy.

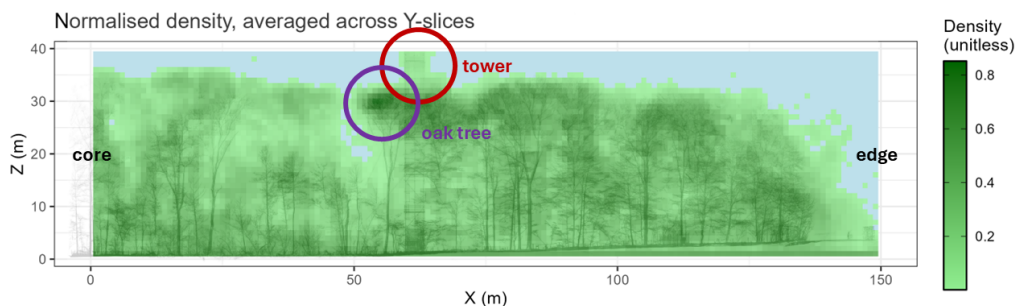


Figure 1: Cross-sectional density plot of 3D grid in 2D

Figure 2 shows the digital terrain model derived from the TLS scans. Along the western side, we

see a small river running from north to south, while on the eastern side, there is a road. The terrain slopes upward from west to east, meaning the road is at a higher elevation than the river. The parallel lines are furrows, a common technique used to improve drainage in wet forests. These furrows are very old and were likely established before the 1650s. Trees could be planted on the elevated, and therefore drier, ridges.

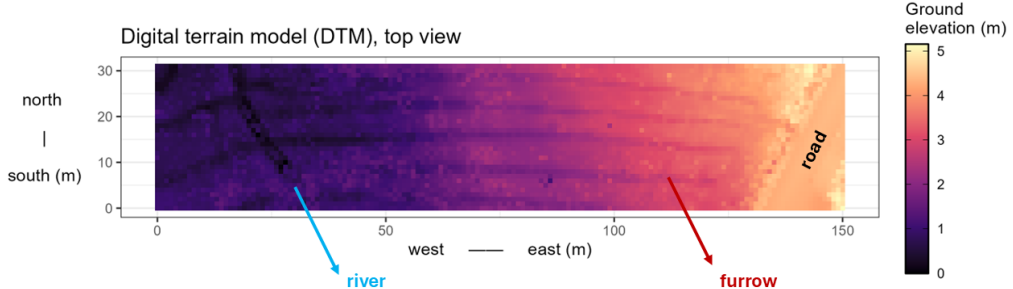


Figure 2

In the simulation discussed below, the microclimate forest surface temperature, air temperature and soil surface temperature are modelled for the location Gontrode in Belgium on July 8, 2023, at 12:00:00 UTC, the hottest day of that year. Input drivers and model parameters similar to the ones mentioned in tables 6 and 5 are used in this simulation.

Figure 3 shows the shortwave direct beam downward radiation for both the vertical and lateral direction (averaged over Y-slices). We observe that light can penetrate deep within the forest gap and is attenuated quite fast in denser canopy areas.

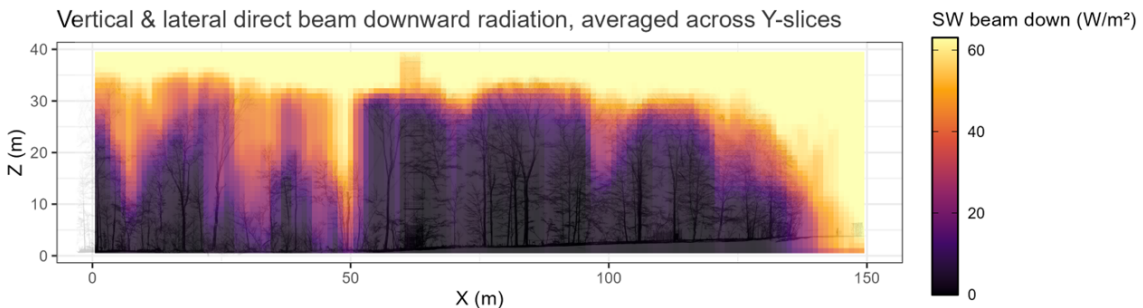


Figure 3

In figure 4, you can see the air temperature averaged over Y-slices along the transect. We see that the macrotemperature outside the forest transect is around 31°C, as expected, since the macrotemperature input driver is set to 31.4°C. At the top of the canopy, we observe warming due to the leaves absorbing and re-emitting radiation. Beneath the canopy, along the ground, there is a clear cooling effect.

Figure 5 displays the surface temperature. Here too, we observe higher temperatures at the top of the canopy and lower temperatures deeper in the forest and along the ground. Compared to the air temperature shown in figure 4, we observe that temperatures in the canopy are higher (up to 35°C). The temperature distribution of the forest surface temperature is wider compared to the one of air temperature.

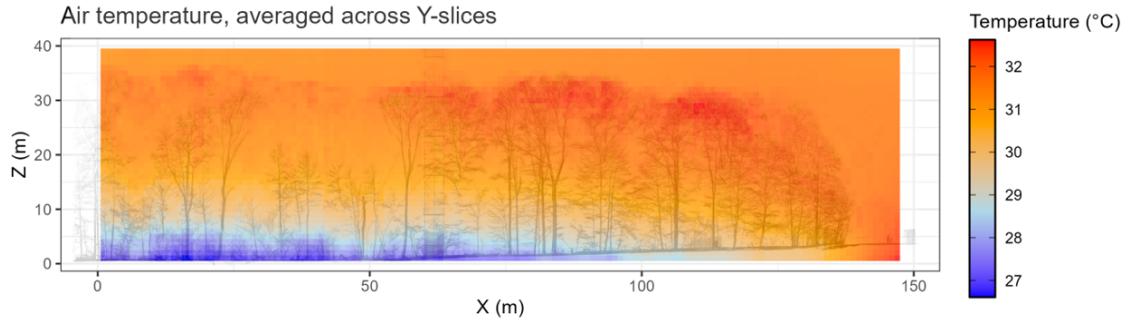


Figure 4

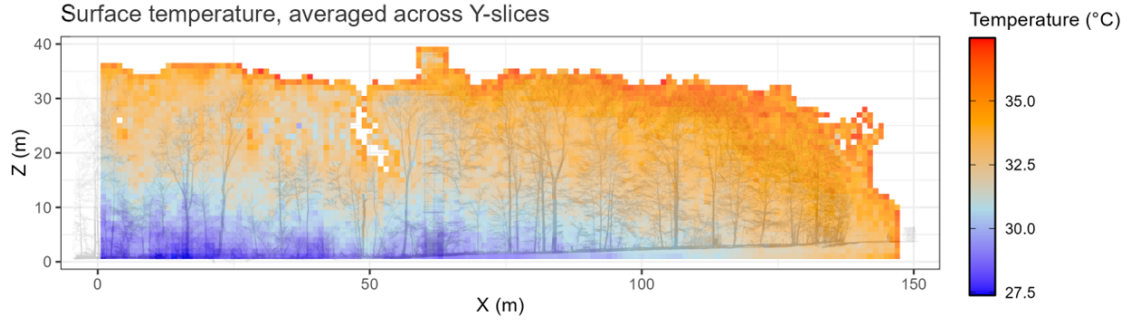


Figure 5

Figure 6 shows the soil surface temperature, just below the lowest Z-grid layer. Here, we observe that the highest temperatures are located at the forest edge, where a road is present. As we move further into the forest, we see a cooling effect, with a slight warming occurring where the forest gap is located.

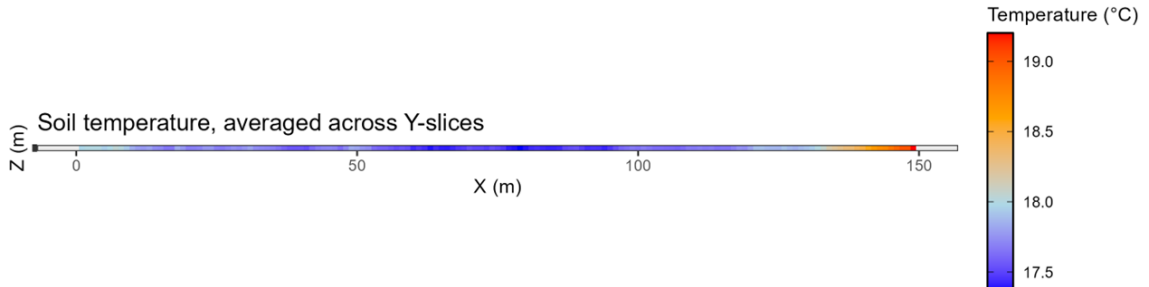


Figure 6

If we then plot the air temperature for the voxels at 1m height along the transect (not averaged over Y-slices, but for the central Y-value, representing the central transect line), we obtain figure 7. Here, we compare the model output in blue with TOMST sensor observations in green. We mainly observe a decrease in temperature from the edge to the interior. This is due to, among other factors, the shading capabilities of the forest, which ensure that radiative heating primarily occurs in the top canopy rather than in the lower structures. Additionally, the heat transfer buffering effect of the forest structure plays a role, bringing warm macroair in along the edge but preventing it from being conducted all the way to the core.

In addition to the horizontal gradient shown in figure 7, figure 8 presents the vertical gradient. The latter is modelled and simulated for the central vertical line of the transect grid and represents

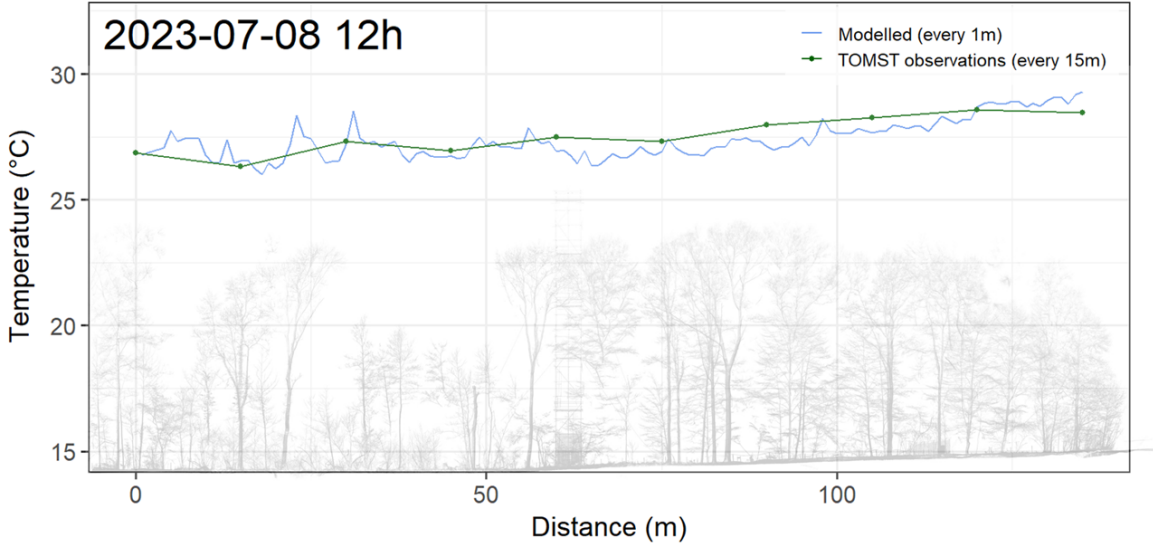


Figure 7: Modelled and observed air temperature at 1m height during a summer day

conditions at 12h PM as well. We observe that temperature increases with increasing height. Just at the top of the canopy, the temperature reaches its maximum, before decreasing again above it.

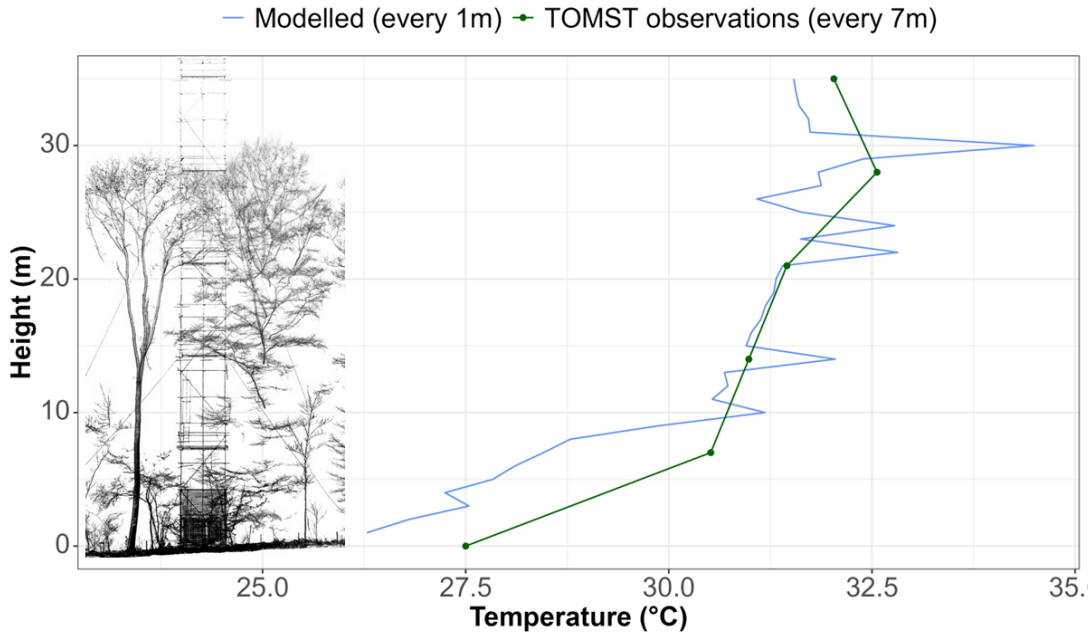


Figure 8: Modelled and observed air temperature along the vertical tower during a summer day

*ForEdgeClim* also produces plots that display the various fluxes. An example of the net radiation flux is shown in figure 9. Here, we see that most radiation is absorbed at the top of the canopy, along the forest edge, and within the gap.

Figure 10 shows the air temperature during a summer night. Compared to figure 7, there are fewer fluctuations, with the most prominent feature being the steady and colder temperature from the forest edge to the core. This corresponds to the expected weaker temperature differences between the forest and the macroenvironment during colder periods.

In Figure 11, we observe an even clearer gradient during the morning of 8 July 2023. Around this time, the sun rises and a relatively large amount of lateral radiation enters along the forest edge

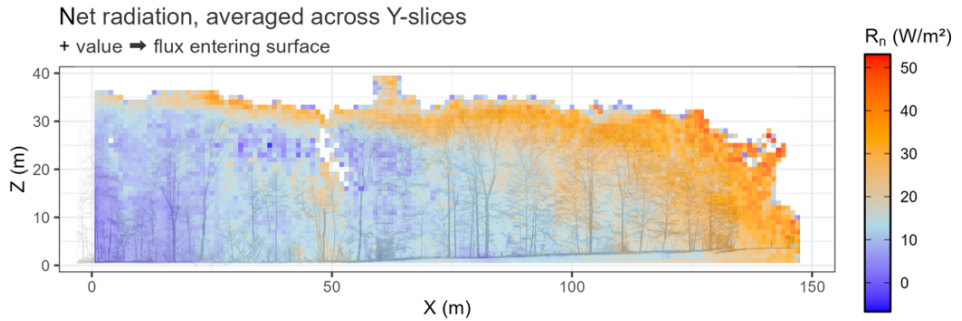


Figure 9

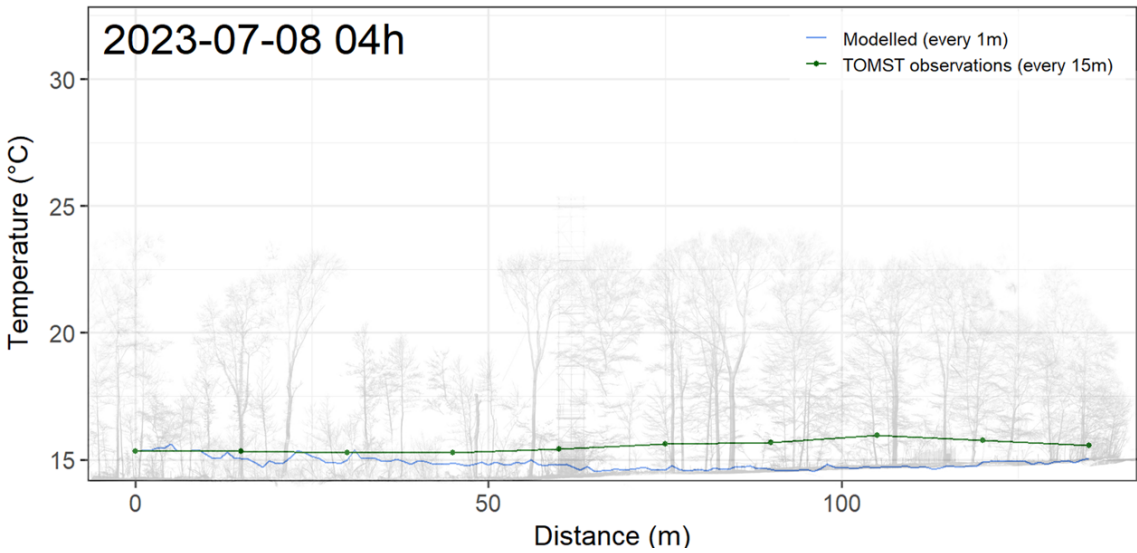


Figure 10: Modelled and observed air temperature at 1m height during a summer night

(eastern side). We can therefore clearly see the effect of lateral radiation in creating a temperature gradient, demonstrating that it is important to include this process in a microclimate model if we wish to account for edge effects. Moreover, there is likely a larger difference in temperature between the area outside and inside the forest during the morning. In the afternoon, for example, the forest has already warmed up, resulting in a less pronounced gradient, but higher absolute temperature values (as seen in figure 7).

If we plot a time series of eight time points on the same warm summer day, 8 July 2023, we obtain Figure 12. Both the model output and the TOMST observations, as well as the forest core and forest edge, are compared. We observe that the temperature near the edge leads that of the core, and that the amplitude (minimum and maximum) of the temperature fluctuations is also greater at the edge than in the core.

## Sensitivity Analysis

As type of sensitivity analysis, we opted for a Sobol analysis (see subsection below for more information on Sobol analysis). We carried this out for four specific months representing the four seasons. Therefore, we selected January (winter), April (spring), July (summer), and October (autumn).

For each seasonal month, and over the years 2023 till 2025, the day with the greatest amount of direct sunlight and the fewest fluctuations in that direct sunlight was identified. The aim was therefore to find the best balance between the hourly mean of direct sunlight and the hourly mean of fluctuations

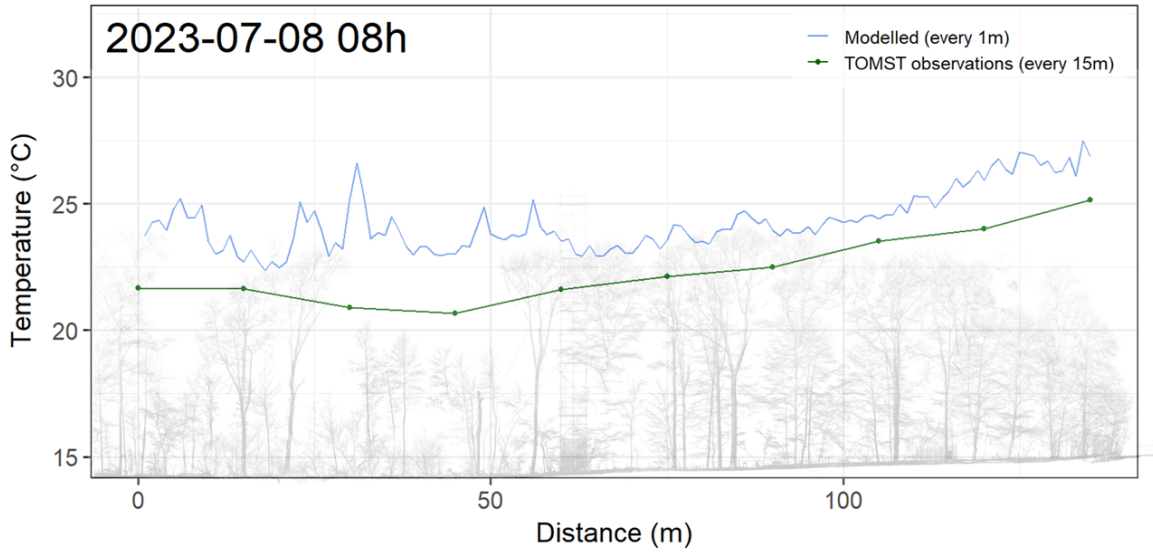


Figure 11: Modelled and observed air temperature at 1m height during a summer morning

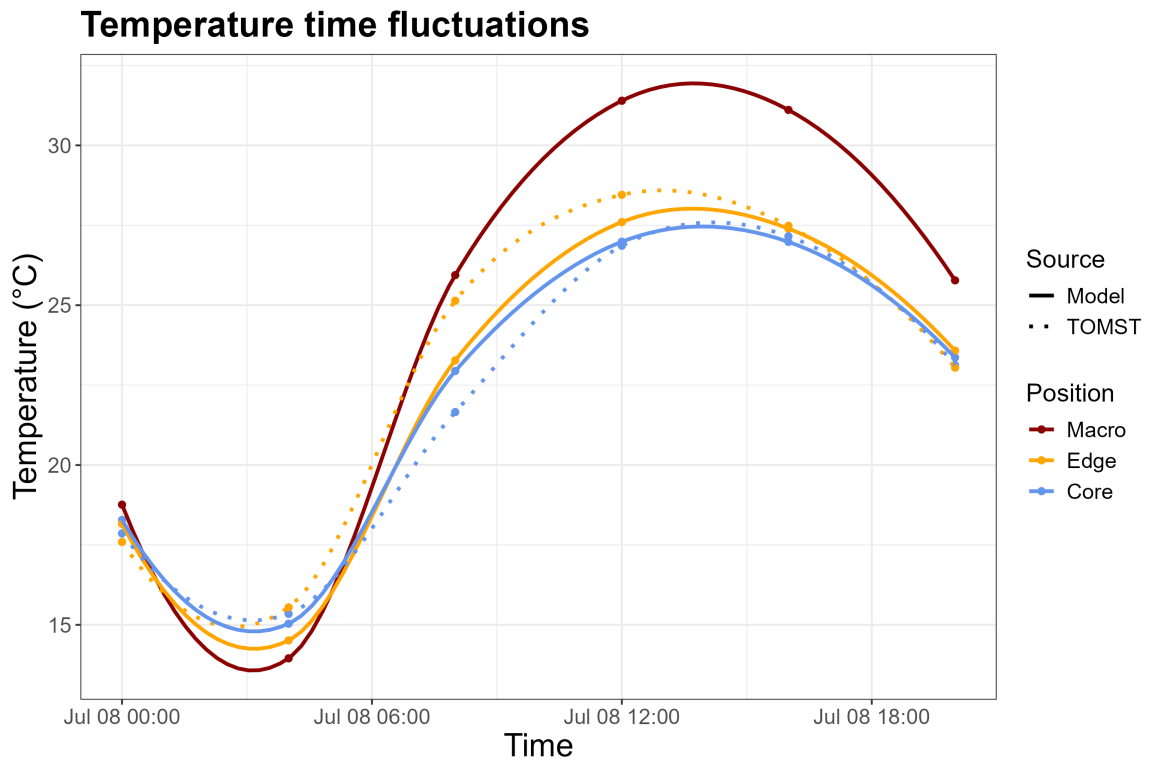


Figure 12: Modelled vs observed and core vs edge air temperature at 1m height during a summer day

in direct sunlight. The hourly mean fluctuations in direct sunlight were defined as the mean absolute difference in direct sunlight between consecutive hours. In this way, days on which the step size (= fluctuation) from one hour to the next remained relatively stable were given more importance. The decision to select the day with the best balance between average direct sunlight and fewest fluctuations in direct sunlight was necessary because our aim with the Sobol analysis is to study the effect of various model parameters on the forest's buffering capacity, and most buffering occurs under high direct solar radiation conditions.

For each of these four sunniest days, we conducted a Sobol analysis for three distinct time points:

in the morning, in the afternoon, and during the night, and this both along the horizontal and vertical line. Here, the horizontal line is defined as the central Y-line along the X-axis at  $Z = 1$  m height. The vertical line is defined as the central X- and Y-line along the Z-axis. The time points were selected based on the number of daylight hours in each season. The morning was defined as approximately one hour after sunrise, the afternoon as the period just after solar noon; and the night-time was consistently set at 1h UTC, as this hour is representative of the night across all seasons. Including the morning time point can be particularly insightful along the horizontal line, as the sun rises in the east and the edge side of the forest is located on the eastern side. By focusing on this morning period in the Sobol analysis, we can examine whether the influence of the parameters changes when lateral radiation penetrates the forest. Furthermore, this morning period is also the onset of warming, whereas the solar noon more or less coincide with the maximum temperature. This all allows us to better analyse the temperature gradient along the transect (both along the horizontal as vertical line) within the Sobol framework. Table 1 shows the exact hours used.

Table 1: Time points per season

Season	Month	Chosen day	Morning ☀	Afternoon ☀	Night ⚡
winter	January	13/01/2025	8h	12h	1h
spring	April	30/04/2025	5h	12h	1h
summer	July	07/07/2023	5h	12h	1h
autumn	October	01/10/2023	6h	12h	1h

After performing the Sobol analysis for each specific season and time point, the Sobol indices were determined for three types of metrics, also referred to as predictor variables. This resulted in  $4 \times 3 \times 3 = 36$  'Quantities of Interest' (QoI), i.e. the number of seasons  $\times$  number of time points  $\times$  number of predictor variables, for both the horizontal and vertical line. The predictor variables considered were the mean temperature, the standard deviation of the temperature, and the temperature gradient.

## Sobol analysis

The Sobol analysis is a global sensitivity analysis technique. It quantifies how much each model parameter contributes to the variance in a model's output, i.e. a predictor variable. There are two main types of indices:

### First-order (= direct-effect) Sobol index ( $S$ )

$$S_i = \frac{Var(\mathbb{E}[Y|X_i])}{Var(Y)} \quad (25)$$

$S_i$  measures the proportion of the total variance in the model output  $Y$  that is explained by variation in parameter  $X_i$  alone, while all other parameters are held constant. It therefore captures the direct influence of parameter  $X_i$  on the output.

### Total-effect Sobol index ( $T$ )

$$T_i = 1 - \frac{Var(\mathbb{E}[Y|X_{\sim i}])}{Var(Y)} \quad (26)$$

with  $X_{\sim i}$  all parameters except  $X_i$ .  $T_i$  measures the total proportion of variance in  $Y$  that is explained by the direct influence of  $X_i +$  all interactions in which  $X_i$  is involved. It therefore answers the question: how important is  $X_i$ , including all its combinations with other parameters?

This analysis is probabilistic: you assign each of your model parameters an uncertainty distribution (for example, uniform between a minimum and maximum), and then sample from those using Monte Carlo or Quasi-Monte Carlo methods. We use the stratified sampling technique of Latin Hypercube Sampling from uniform parameter distributions and used 400 parameter sampling sets. For each model parameter, typical value ranges were identified from the literature. Table 5 shows the typical value ranges ( $U(\min, \max)$ ).

## Results sensitivity analysis along the horizontal line

Figures 13 and 14 show the extent to which each model parameter contributes to the variance for each Quantity of Interest along the horizontal line. Figure 13 distinguishes between parameters related to shortwave radiation (yellow colour range), longwave radiation (purple colour range), and heat transfer (green colour range). Figure 14 is a copy of figure 13, retaining only the heat transfer parameters, each of which has been assigned a more clearly distinguishable colour.

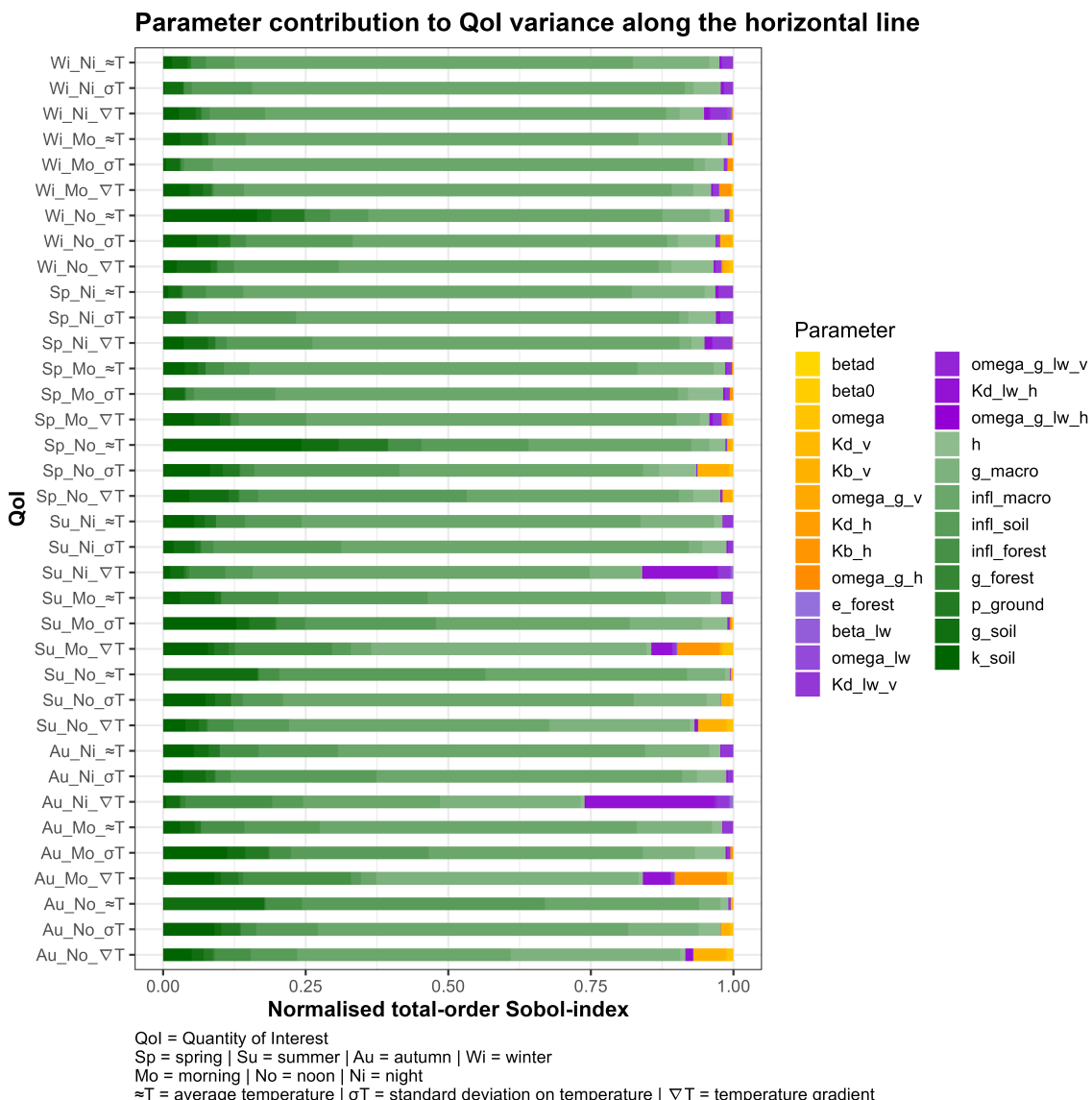


Figure 13

If we then refer to the 3 metrics, the 3 times of day, and the 4 seasons as 'conditions', we can calculate the average contribution of the key (= heat transfer) parameters for each condition. Figures 15 and 16 display these. Similar to the figures related to the Quantities of Interest, figure 15 distinguishes

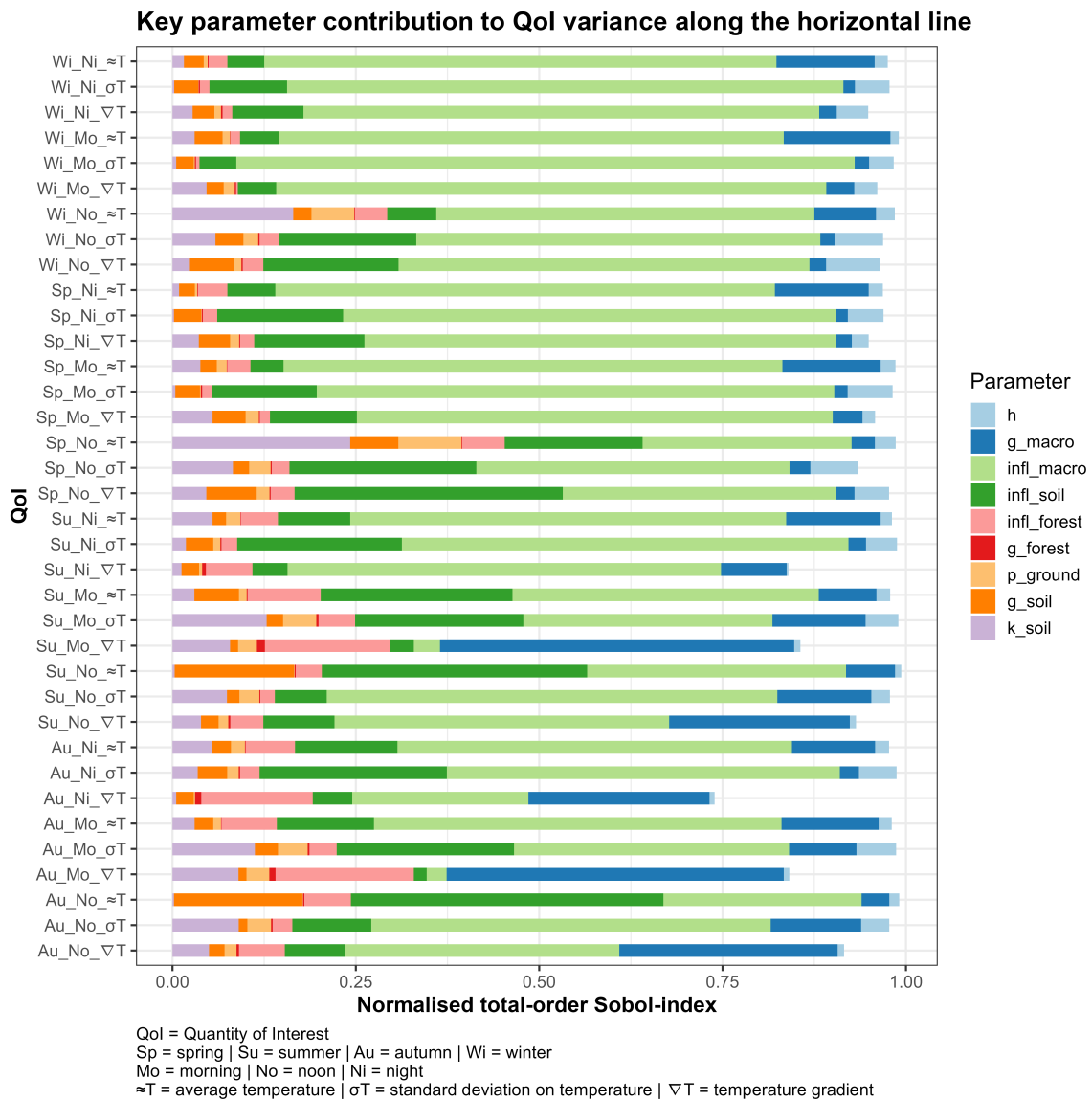


Figure 14

between parameters related to shortwave radiation (yellow colour range), longwave radiation (purple colour range), and heat transfer (green colour range). Figure 16 is a copy of figure 15, retaining only the heat transfer parameters, each of which has been assigned a more clearly distinguishable colour.

Across all conditions, heat transfer parameters, particularly  $\text{infl}_{\text{macro}}$ ,  $\text{infl}_{\text{soil}}$ , and  $\text{g}_{\text{macro}}$ , dominate model output sensitivity. For each condition, these top three parameters explain between 71% and 83% of output variance, indicating that sensitivity is concentrated in a small subset of model parameters. Furthermore, and again across all conditions, the standard deviation on the parameter rank of the top three parameters is very low (between 0 and 2.6), indicating that their relative importance is robust across conditions.

Shortwave and longwave processes contribute minimally. However, when looking at the times of day, we see that longwave radiation has the greatest influence during the night, and shortwave radiation during the day. Across the seasons, longwave contributes the most in autumn, and shortwave the most in spring. Across the metrics, radiation in general contributes the most to the temperature gradient. This makes sense, as the temperature gradient runs from forest edge to forest core and radiation is simulated as entering along the forest edge.

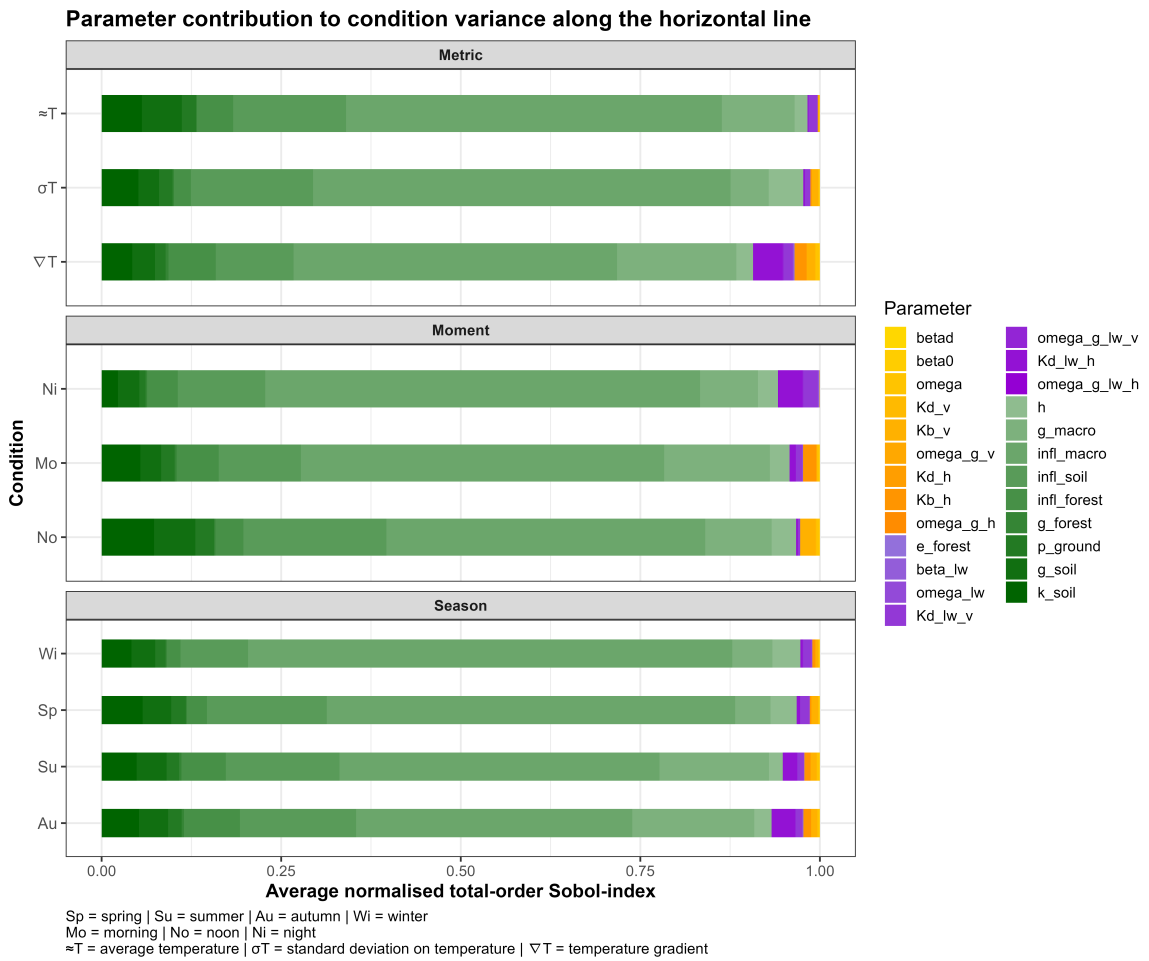


Figure 15

In addition to the normalised Sobol indices, we also examined the non-normalised output. This was, however, very similar; that is, the absolute importance of the different parameters in explaining model sensitivity does not change substantially across the various Quantities of Interest. Figure 17 for example shows the same results as in figure 14 but with the absolute Sobol indeces on the horizontal axis.

## Results sensitivity analysis along the vertical line

When running the sensitivity analysis for the vertical line, we obtain very similar results. Across all conditions, the same three heat-transfer parameters,  $infl_{macro}$ ,  $infl_{soil}$ , and  $g_{macro}$  dominate model output sensitivity. Compared with the horizontal line, they account for an even larger share of the output variance, namely between 78 and 91%. Here too, across all conditions, the standard deviation of the parameter rank for the top three parameters is very low (between 0 and 2.2), indicating that their relative importance is robust across conditions.

Shortwave and longwave processes contribute even less than in the horizontal sensitivity analysis. You can see this by comparing figure 18 with 15, showing the parameter contribution to condition variance along the vertical and horizontal line respectively.

Radiative transfer parameters might be less important in the vertical direction because of rapid attenuation of shortwave radiation and rapid equilibration of longwave radiation, whereas in the ho-

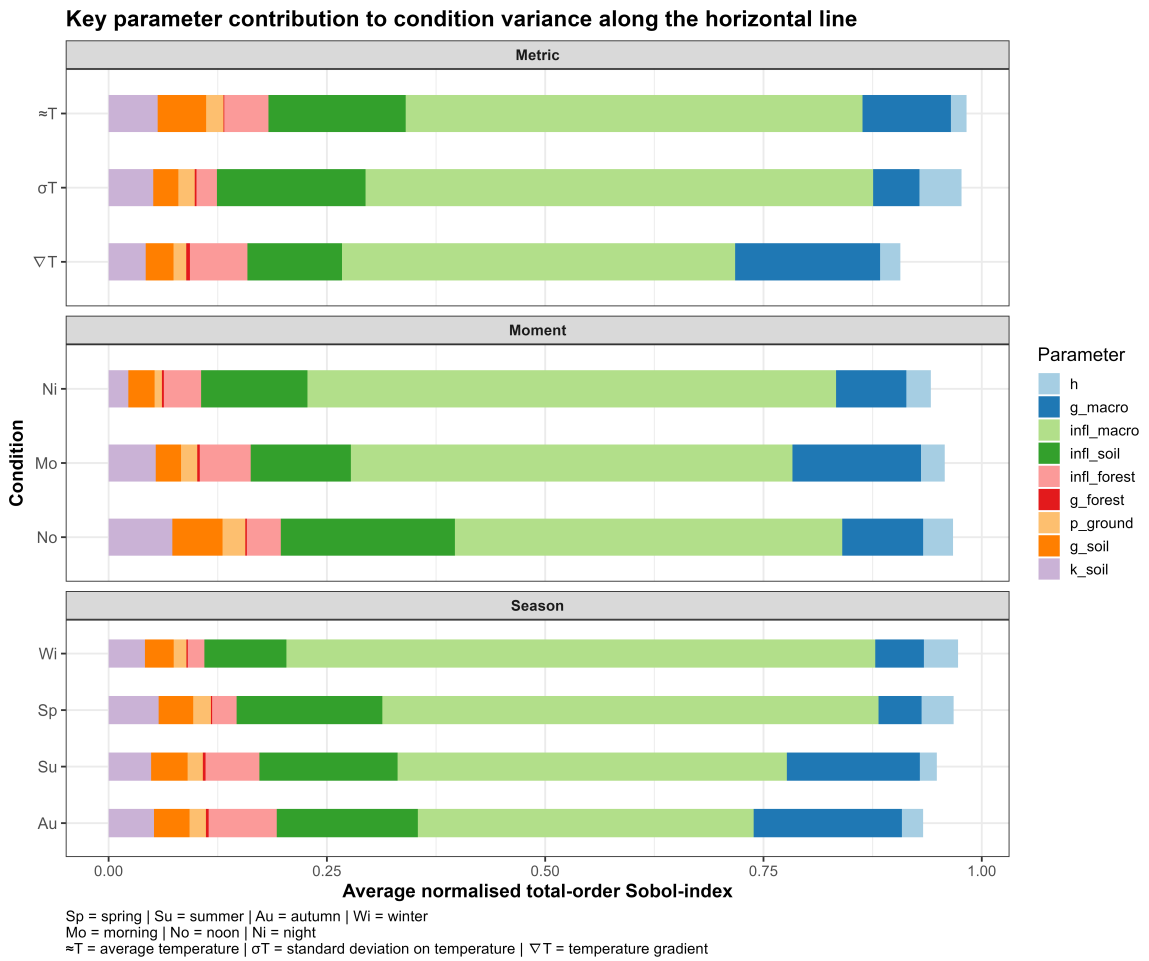


Figure 16

horizontal direction, longer path lengths, greater structural heterogeneity, and stronger edge contrasts make both shortwave and longwave fluxes more sensitive to parameter values.

Based on these findings from the sensitivity analysis, we can focus on the top three parameters for the calibration process. For the remaining 22 parameters, we will use a fixed value, namely the mean value from the uniform distribution as reported in the literature (see table 5).

## Calibration

As a calibration algorithm, we selected the Covariance Matrix Adaptation - Evolution Strategy (CMA-ES; Hansen & Ostermeier, 2001; see subsection below for more information on the CMA-ES algorithm). The calibration procedure was performed separately for each season, resulting in four independent calibrations. For each calibration, we used data from a 24-hour period on 3 specific days. In addition to the sunniest day (as shown in table 1), we also calibrated for the cloudiest day and the day with the greatest solar fluctuations. The cloudiest day, for each seasonal month across the years 2023 to 2025, was defined as the day, over all daylight hours, with the highest amount of clouded hourly timesteps (tolerance of 5 W/m<sup>2</sup> was set on the difference between total and diffuse radiation). The day with the greatest solar fluctuations was defined analogously for each seasonal month across the years 2023 to 2025, but this time as the day on which the largest number of shifts occurred between a clouded hour (difference between total and diffuse radiation is minimal, tolerance set at 5 W/m<sup>2</sup>) and an hour with direct solar radiation. The results for the sunniest days and these clouded days and days with the greatest solar fluctuations are presented in table 2. The objective function to be minimised was the

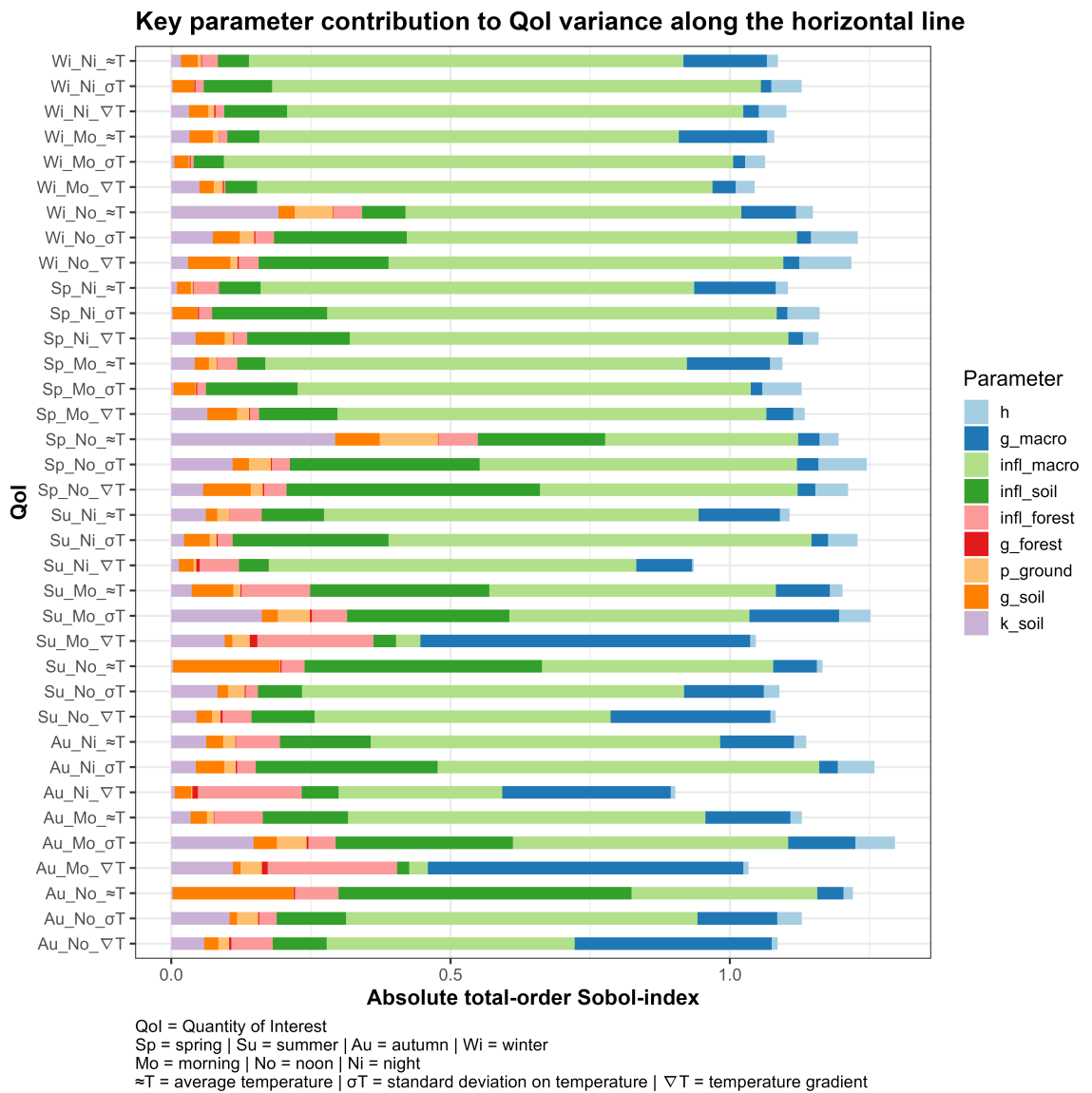


Figure 17

Root Mean Square Error (RMSE) between simulated and observed air temperatures. Observations for each hour were obtained from 15 sensors in total: 10 positioned horizontally along the forest transect and 5 mounted vertically along a tower. Like this, we had  $3 \times 24 \times 15 = 1080$  model/observation pairs on which the RMSE was calculated. Apart from capturing several light conditions within the calibration procedure, this setup furthermore ensures that the calibration accounts for both horizontal and vertical variability in microclimate conditions.

The TOMST TMS sensors that we use to observe forest temperature may be subject to sunflecks. That is, when direct sunlight falls on the sensor, it becomes undesirably heated and no longer records the correct air temperature within the forest. For all 24-hour steps of the days shown in table 2, the TMS data were manually checked for sunflecks. For all cloudiest days and days with the greatest solar fluctuations, no sunflecks were observed. However, on the sunniest summer day (07/07/2025), sunflecks were recorded at 10:00 UTC and 11:00 UTC for one of the the ground sensors, namely the one in the most open canopy area. These two data points were therefore excluded from the calibration analysis.

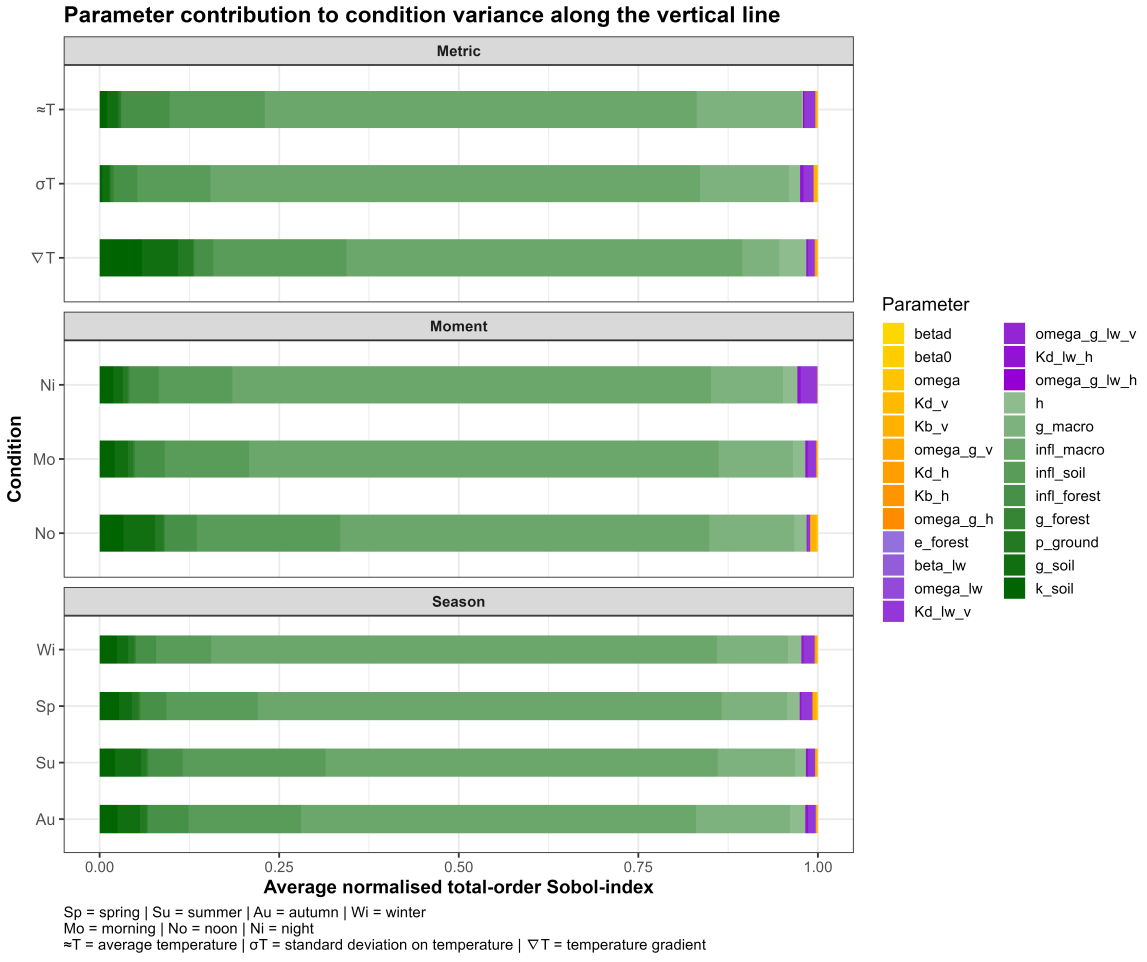


Figure 18

Table 2: Three specific days per season

Season	Month	Most sunny day	Most cloudy day	Most solar fluctuating day
winter	January	13/01/2025	20/01/2025	23/01/2025
spring	April	30/04/2025	23/04/2025	02/04/2024
summer	July	07/07/2023	31/07/2023	20/07/2023
autumn	October	01/10/2023	09/10/2024	19/10/2023

## Covariance Matrix Adaptation - Evolution Strategy (CMA-ES)

CMA-ES is a stochastic, derivative-free evolutionary optimisation algorithm that is well suited for non-linear and non-convex objective functions, especially when the search space is complex, discontinuous, or contains multiple local optima. These characteristics make it particularly suitable for calibrating process-based environmental models, where the objective function is often non-smooth and derivative information is unavailable or unreliable. In addition, CMA-ES has been shown to perform robustly in relatively low-dimensional parameter spaces, which matches the scope of our calibration problem.

The algorithm operates by iteratively updating a multivariate normal distribution from which new candidate parameter sets are sampled:

$$x \sim \mathcal{N}(m, \sigma^2 C)$$

where  $m \in \mathbb{R}^n$  is the mean vector (current best parameter estimate),  $\sigma$  is the global step-size, and

$C \in \mathbb{R}^{n \times n}$  is the covariance matrix controlling the shape and orientation of the search distribution.  $n$  is the amount of parameters to be optimized.

Each iteration starts with a set of ‘parent’ parameter vectors representing the current search distribution. From these, a population of ‘offspring’ is generated by random sampling from the multivariate normal distribution. The objective function is evaluated for each offspring, after which the best-performing candidates are selected to form the new generation. This selection updates both the mean vector and the covariance matrix. The adaptation of the covariance matrix allows the algorithm to learn correlations between parameters and to bias exploration towards the most promising regions of the search space, while avoiding premature convergence. In our application, CMA-ES was run for 30 generations (7 offspring per generation => 210 iterations) for the summer season, 40 generations for spring and 50 generations for both autumn and winter. The difference in the number of generations is due to the fact that the convergence of the algorithm varied between the seasons. For summer, 30 generations were sufficient for the algorithm to converge, whereas for winter we needed 50 generations.

### Role and adaptation of the covariance matrix

The covariance matrix  $C$  encodes both the spread of the distribution in each parameter direction and the correlations between parameters:

- The diagonal elements  $C_{ii}$  represent the variances of the individual parameters.
- The off-diagonal elements  $C_{ij}$  represent covariances, indicating how changes in parameters  $i$  and  $j$  tend to co-occur.

CMA-ES’s ability to adapt these covariances is key to its efficiency, as it allows the search distribution to align with curved or tilted ridges (or troughs) in the objective function landscape.

After selecting the best-performing offspring, CMA-ES computes weighted step vectors:

$$y_k = \frac{x_k - m}{\sigma}$$

and updates the covariance matrix as:

$$C \leftarrow (1 - c_{\text{cov}}) C + c_{\text{cov}} \sum_{k=1}^{\mu} w_k y_k y_k^\top$$

where  $c_{\text{cov}}$  is a learning rate,  $\mu$  is the number of selected candidates (best offspring sets), and  $w_k$  are positive weights summing to one. This update increases variance along directions with repeated success and reduces it elsewhere, transforming the search distribution from an initial isotropic sphere to an ellipsoid aligned with the most promising principal components.

### Principal components and eigen decomposition

The covariance matrix can be decomposed as:

$$C = Q \Lambda Q^\top$$

where  $Q$  contains the eigenvectors  $v_1, v_2, \dots, v_n$  (principal components, or search directions), and  $\Lambda = \text{diag}(\lambda_1, \dots, \lambda_n)$  contains the eigenvalues. A larger eigenvalue indicates greater variance and thus more exploration in the corresponding search direction. In an  $n$ -dimensional search space, there are  $n$  principal components. CMA-ES explores all of them, but with more intensity along those with higher eigenvalues, as these correspond to directions offering the highest potential for improvement. The largest eigenvalue defines the main search direction.

## Results calibration

Table 3 presents the calibrated parameter values and corresponding RMSE per season.

Table 3: Calibrated parameters

season \ parameter	$g_m (W/m^2/K)$	$i_m (m)$	$i_s (m)$	RMSE ( $^{\circ}C$ )
winter	35.64	46.06	0.037	1.28
spring	39.80	59.67	5.65	1.56
summer	25.28	39.26	6.40	1.23
autumn	39.61	18.49	9.97	1.10

For the summer, we ran the CMA-ES algorithm for 30 generations, and figures 19 and 20 illustrate how the algorithm converged over the generations.

Figure 19 shows the RMSE across all generations and offspring. The pink dotted line in this figure indicates the best RMSE for each generation. We observe that the RMSE decreases as the generations progress and then plateaus. This indicates that no better fit can be found and demonstrates that the algorithm has converged.

Figure 20 also illustrates the convergence of the algorithm. In this figure, a Principal Component Analysis (PCA) was performed on the complete dataset of parameter sets, containing all generations (including offspring). This allowed us to define two main PCs and compare generations with one another. The figure clearly shows that, as the generations progress, the spread of the parameters in the parameter space decreases. This is another sign of convergence.

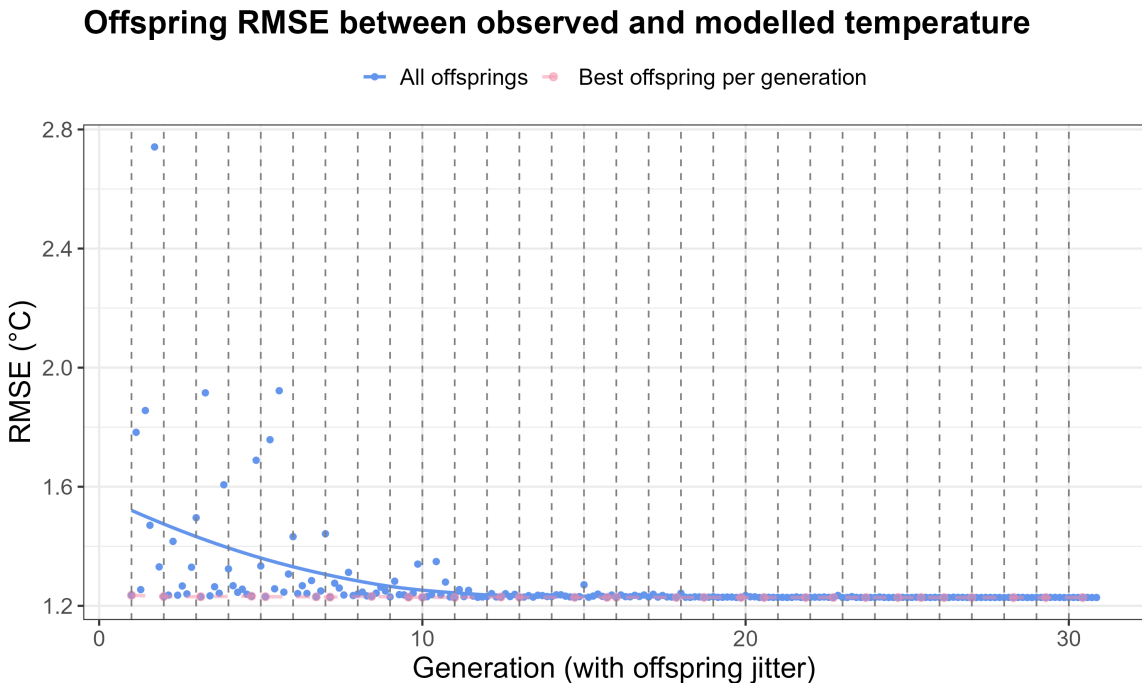


Figure 19

### CMA-ES population spread per generation

Points = offspring,  
Ellipse = 95% spread

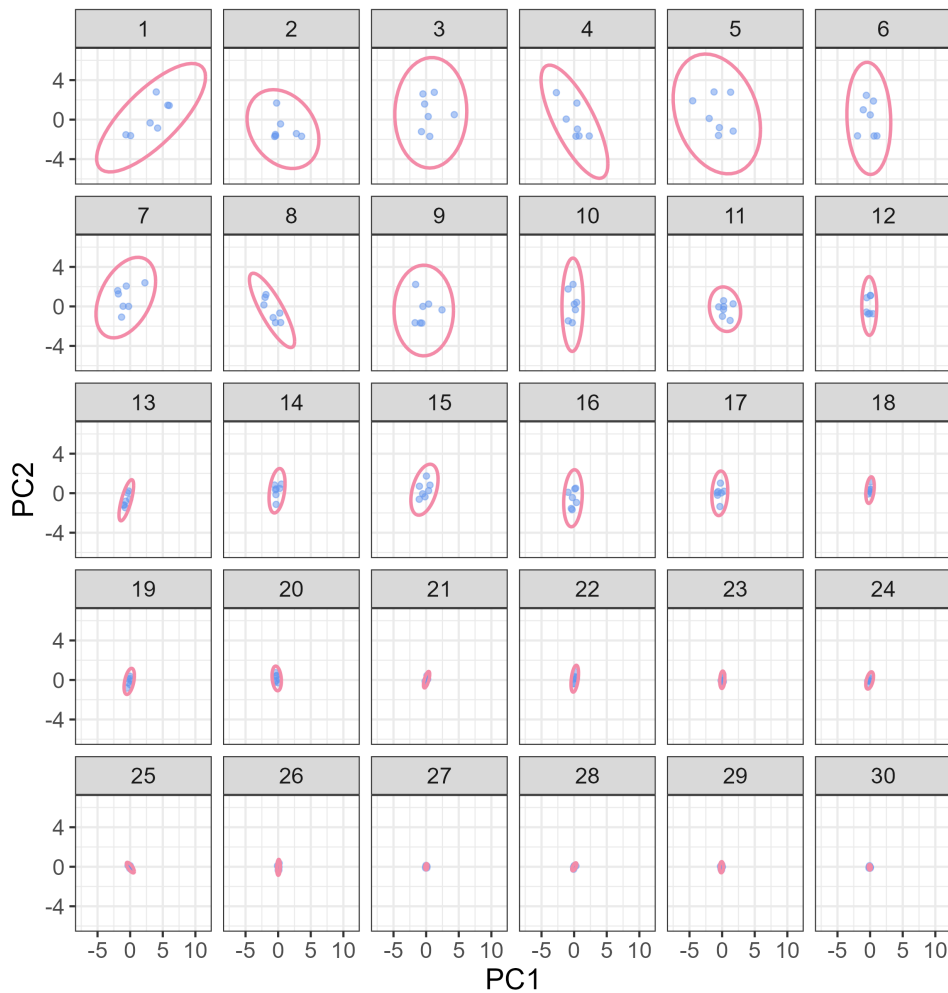


Figure 20

## Validation

The model was validated per season on all days of the month, from which the sunniest day was extracted. This choice of month is arbitrary but ensures that we capture a range of different light conditions. For summer this is July 2023, for autumn October 2023, for winter January 2025, and for spring April 2025. In this way, we consider 30 (or 31) days  $\times$  24 time steps  $\times$  15 positions = 10800 validation points per season. The model was run with calibrated values (i.e. for the top three parameters) and with uncalibrated values. The uncalibrated values are the averages of the parameter distributions reported in the literature (see also table 5).

For the winter season, figure 21 shows the model output wrt the observed air temperatures for both the calibrated model and the uncalibrated model. We see that the calibrated model performs better, with a higher  $R^2$  and NSE (Nash-Sutcliffe model efficiency coefficient). The same is true for figure 22 where we can see a time series of the residuals between modelled and observed air temperature. The calibrated model shows a better performance with a lower RMSE (root mean square error) and ME (mean error).

For the summer season we don't have this clear distinction between calibrated and uncalibrated model. There is less difference because the calibrated parameter set does not differ much from the average parameter values as found in literature. All statistical measures for the 4 seasons are given in table 4. In general however, there does not seem to be a lot of difference between the calibrated and the uncalibrated model, both perform well for all seasons.

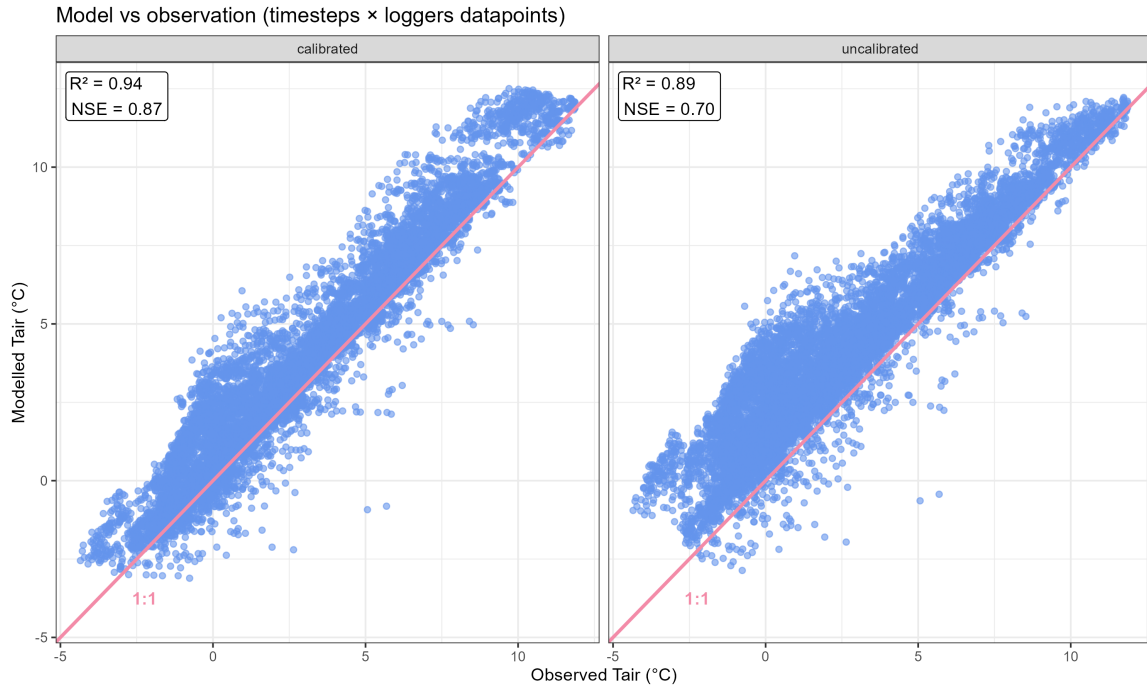


Figure 21

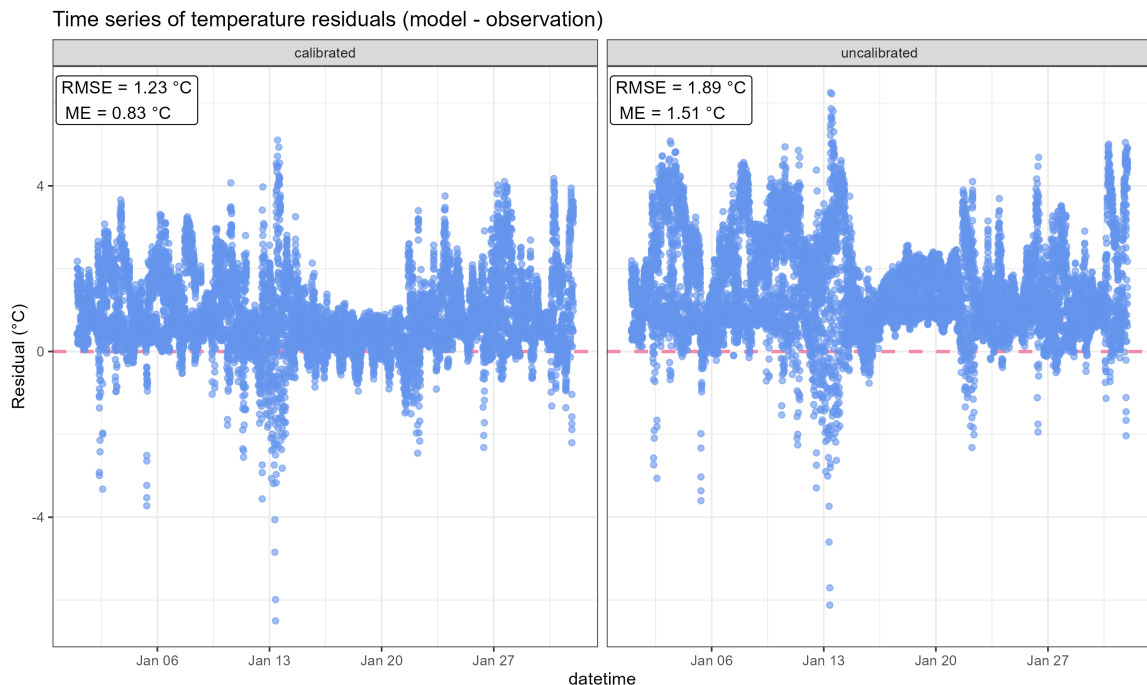


Figure 22

Table 4: Statistical measures of the validation for the calibrated and uncalibrated model for the four seasons

season	calibrated				uncalibrated			
	$R^2$	NSE	RMSE (°C)	ME (°C)	$R^2$	NSE	RMSE (°C)	ME (°C)
winter	0.94	0.87	1.23	0.83	0.89	0.70	1.89	1.51
spring	0.86	0.85	2.05	0.41	0.87	0.84	2.14	0.86
summer	0.93	0.90	1.06	0.57	0.93	0.90	1.07	0.59
autumn	0.94	0.83	1.52	1.21	0.95	0.84	1.48	1.21

## Final remarks

The *ForEdgeClim* model, as described in this report, aims to simulate microclimate/ -temperature in a (temperate) forest in a physically realistic manner, given macroinput drivers and forest structure. To achieve this, key contributing processes were identified and considered in terms of how they could be modelled in a physically accurate way. When selecting processes and their mathematical implementation, a balance was sought between detail and relevance.

*ForEdgeClim* is therefore not an extremely detailed microclimate model that accounts for all microclimatic ecosystem processes. However, the model currently appears to generate physically realistic output. In future versions, processes such as a more detailed soil heat flux, (lateral) wind, and hydrological processes seem to be among the top priorities for inclusion.

## References

- *microcimf* model by Ilya Maclean
- *SCOPE 2.0* model by Wim Verhoef & Christiaan van der Tol
- *ED 2.2* model by the *ED 2.2* development team

Table 5: Model parameters

name	explanation	U(min, max)	unit	submodel
$K_{b-v}$	direct beam radiation extinction coefficient in vertical direction	[0.5, 2]		
$K_{d-v}$	diffuse radiation extinction coefficient in vertical direction	[0.6, 0.95]		
$K_{b-h}$	direct beam radiation extinction coefficient in lateral direction	[0.3, 2]	unitless	SW RTM
$K_{d-h}$	diffuse radiation extinction coefficient in lateral direction	[0.5, 0.95]		
$\beta_0$	fraction of scattered direct beam radiation in backward direction	[0.2, 0.45]		
$\beta$	fraction of scatterd diffuse radiation in backward direction	[0.3, 0.35]		
$\omega$	shortwave scattering coefficient	[0.43, 0.61]		
$\omega_{g-v}$	shortwave ground scattering	[0.08, 0.18]		
$\omega_{g-h}$	shortwave scattering by the inner forest	[0.1, 0.2]		
$\epsilon_f$	emissivity of the forest	[0.94, 0.99]		
$K_{l-v}$	longwave radiation extinction coefficient in vertical direction	[0.2, 0.4]	unitless	LW RTM
$K_{l-h}$	longwave radiation extinction coefficient in lateral direction	[0.2, 0.4]		
$\beta_l$	fraction of scatterd longwave radiation in backward direction	[0.3, 0.35]		
$\omega_l$	longwave scattering coefficient	[0.01, 0.06]		
$\omega_{lg-v}$	longwave ground scattering	[0.04, 0.07]		
$\omega_{lg-h}$	longwave scattering by the inner forest	[0.01, 0.06]		
$h$	diffusion coefficient of air	[0, 20]	$W/m^2/K$	H
$p$	fraction of net radiation at ground level to define ground heat flux	[0.1, 0.35]	unitless	G
$g_s$	convection coefficient between air and soil surface	[5, 15]	$W/m^2/K$	$T_{air}$
$g_f$	convection coefficient between air and forest structure	[5, 20]	$W/m^2/K$	$T_{air}$ & H
$g_m$	convection coefficient between air and macroenvironment	[10, 40]	$W/m^2/K$	$T_{air}$
$i_s$	distance over which the influence of $T_s$ on $T_{air}$ is reduced bij 50%	[0, 10]	m	$T_{air}$
$i_f$	distance over which the influence of $T_f$ on $T_{air}$ is reduced bij 50%	[0, 10]	m	$T_{air}$
$i_m$	distance over which the influence of $T_{macro}$ on $T_{air}$ is reduced bij 50%	[5, 60]	m	$T_{air}$
$k_s$	thermal conductance of the soil	[0.25, 2.2]	$W/m/K$	$T_s$

Table 6: Input drivers (and spacetime specifics)

name	explanation	example value	unit
$T_{macro}$	macrotemperature at top canopy	31	°C
$T_{soil}$	soil temperature at 6cm depth	17	°C
$I_{sky,b}^\downarrow$	downward direct beam radiation at top canopy	600	$W/m^2$
$I_{sky}^\downarrow$	downward diffuse radiation at top canopy	200	$W/m^2$
$L_{sky}^\downarrow$	downward longwave radiation at top canopy	400	$W/m^2$
$\rho$	voxelised density from TLS point cloud	0.5	unitless
lat	latitude of forest site	50.980	°
long	longitude of forest stite	3.816	°
datetime	date & time of simulation/observation	2023-07-08 12:00:00	UTC

Table 7: (Physical) constants

name	explanation	value	unit	submodel
$\sigma$	Stefan-Boltzmann constant	5.67e-8	$W/m^2/K^4$	LW RTM
voxel size	length of the edge of a voxel cube	1	$m$	H
$c_p$	specific heat of air	1000	$J/kg/K$	H
$\rho_{air}$	air density	1.225	$kg/m^3$	H
$\alpha$	Priestley-Taylor coefficient	1.26	unitless	LE
$\gamma$	psychrometric constant	0.066	$kPa/K$	LE

Table 8: Prognostic variables (model outputs)

These outputs are modelled for each voxel at the steady state.

name	explanation	example value	unit
$T_f$	temperature of forest structure	28	°C
$T_s$	temperature of soil surface	21	°C
$T_{air}$	temperature of forest air	25	°C
$R_n$	net radiation flux	20	$W/m^2$
$H$	sensible heat flux	20	$W/m^2$
$LE$	latent heat flux	20	$W/m^2$
$G$	ground heat flux	20	$W/m^2$
$I_b^\downarrow$	downward direct beam radiation flux	20	$W/m^2$
$I^\downarrow$	downward diffuse radiation flux	20	$W/m^2$
$I^\uparrow$	upward diffuse radiation flux	20	$W/m^2$
$L^\downarrow$	downward longwave radiation flux	20	$W/m^2$
$L^\uparrow$	upward longwave radiation flux	20	$W/m^2$